AFRL-VA-WP-TP-2006-333

HYPERSONIC INLET WITH PLASMA INDUCED COMPRESSION (POSTPRINT)

J.S. Shang, J. Menart, Roger L. Kimmel, and J. Hayes

JANUARY 2006

Approved for public release; distribution is unlimited.

STINFO COPY

AIR VEHICLES DIRECTORATE
AIR FORCE MATERIEL COMMAND
AIR FORCE RESEARCH LABORATORY
WRIGHT-PATTERSON AIR FORCE BASE, OH 45433-7542

NOTICE AND SIGNATURE PAGE

AFRL-VA-WP-TP-2006-333 HAS BEEN REVIEWED AND IS APPROVED FOR PUBLICATION IN ACCORDANCE WITH ASSIGNED DISTRIBUTION STATEMENT.

*//Signature//	//Signature//
ROGER L. KIMMEL	CARL P. TILMANN
Senior Research Engineer	Acting Chief
Aeroconfiguration Research Branch	Aeroconfiguration Research Branch

*Disseminated copies will show "//signature//" stamped or typed above the signature blocks.

REPORT DOCUMENTATION PAGE

Form Approved
OMB No. 0704-0188

1. REPORT DATE *(DD-MM-YY)*	2. REPORT TYPE	3. DATES COVERED *(From - To)*
January 2006	Conference Paper Postprint	01/01/2001 – 01/01/2006

4. TITLE AND SUBTITLE
HYPERSONIC INLET WITH PLASMA INDUCED COMPRESSION (POSTPRINT)

5a. CONTRACT NUMBER
In-house

5b. GRANT NUMBER

5c. PROGRAM ELEMENT NUMBER
61102F

6. AUTHOR(S)
J.S. Shang and J. Menart (Wright State University)
Roger L. Kimmel and J. Hayes (AFRL/VAAA)

5d. PROJECT NUMBER
A03U

5e. TASK NUMBER

5f. WORK UNIT NUMBER
0B

7. PERFORMING ORGANIZATION NAME(S) AND ADDRESS(ES)

Wright State University
Mechanical and Materials Department
Dayton, OH 45435

Aerodynamic Configuration Branch (AFRL/VAAA)
Aeronautical Sciences Division
Air Vehicles Directorate
Air Force Materiel Command, Air Force Research Laboratory
Wright-Patterson Air Force Base, OH 45433-7542

8. PERFORMING ORGANIZATION REPORT NUMBER
AFRL-VA-WP-TP-2006-333

9. SPONSORING/MONITORING AGENCY NAME(S) AND ADDRESS(ES)

Air Vehicles Directorate
Air Force Research Laboratory
Air Force Materiel Command
Wright-Patterson Air Force Base, OH 45433-7542

10. SPONSORING/MONITORING AGENCY ACRONYM(S)
AFRL-VA-WP

11. SPONSORING/MONITORING AGENCY REPORT NUMBER(S)
AFRL-VA-WP-TP-2006-333

12. DISTRIBUTION/AVAILABILITY STATEMENT
Approved for public release; distribution is unlimited.

13. SUPPLEMENTARY NOTES

Conference paper published in the Proceedings of the 2006 44th AIAA Aerospace Sciences Meeting and Exhibit, published by AIAA. PAO Case Number: AFRL/WS 05-2820 (cleared 28 Dec 2005). Paper contains color.

14. ABSTRACT

A path-finding experimental investigation has been successfully accomplished to show the combined effect of an electromagnetic perturbation and viscous-inviscid interaction is a viable mechanism for improving hypersonic inlet performance. The plasma-induced compression is produced by a direct current discharge from electrodes embedded in the sidewalls of a rectangular constant cross-sectional area inlet. This repeatable compression acts as the sidewall compression of a variable area inlet but without the parasitic effect when deactivated. The accompanying numerical simulation is first calibrated with the measured Pitot pressures and then used to evaluate the overall flow structure within the inlet. The magneto-fluid-dynamics interaction is found to be unsteady and characterized with low amplitude and high frequency fluctuations. The validated result reveals that a plasma generating power supply of 19.12 watts per centimeter of electrode length produces an 11.6% pressure rise at the inlet exit.

15. SUBJECT TERMS

16. SECURITY CLASSIFICATION OF:			17. LIMITATION OF ABSTRACT:	18. NUMBER OF PAGES	19a. NAME OF RESPONSIBLE PERSON (Monitor)
a. REPORT	b. ABSTRACT	c. THIS PAGE			Roger L. Kimmel
Unclassified	Unclassified	Unclassified	SAR	18	19b. TELEPHONE NUMBER *(Include Area Code)* N/A

Standard Form 298 (Rev. 8-98)
Prescribed by ANSI Std. Z39-18

AIAA 2006-0764

Hypersonic Inlet with Plasma Induced Compression

J.S. Shang*, J. Menart*, R. Kimmel**, and J. Hayes**

Mechanical and Materials Department*
Wright State University
Dayton, OH 45435

Air Vehicles Directorate**
Air Force Research Laboratory
WPAFB, OH

Abstract

A path-finding experimental investigation has been successfully accomplished to show the combined effect of an electromagnetic perturbation and viscous-inviscid interaction is a viable mechanism for improving hypersonic inlet performance. The plasma-induced compression is produced by a direct current discharge from electrodes embedded in the sidewalls of a rectangular constant cross-sectional area inlet. This repeatable compression acts as the sidewall compression of a variable area inlet but without the parasitic effect when deactivated. The accompanying numerical simulation is first calibrated with the measured Pitot pressures and then used to evaluate the overall flow structure within the inlet. The magneto-fluid-dynamics interaction is found to be unsteady and characterized with low amplitude and high frequency fluctuations. The validated result reveals that a plasma generating power supply of 19.12 watts per centimeter of electrode length produces an 11.6% pressure rise at the inlet exit.

Nomenclature

B Magnetic field intensity
E Electrical field intensity
J Electrical current density
n Number density of charged particles
R_m Magnetic Reynolds number, $UL/(\mu_m\sigma)^{-1}$
u Velocity vector (u,v,w)
$\boldsymbol{\tau}$ Shear stress tensor
ε Electrical permittivity
μ_m Magnetic permeability
ρ Density
φ Electrical potential
σ Electrical conductivity
$\boldsymbol{\Gamma}$ Flux vector of charged particle number density

I. Introduction

In an air-breathing propulsive system, the inlet ingests ambient air from the oncoming stream and compresses it to a higher temperature and pressure for the combustor. The optimal performance for a high-speed inlet is reached when the Mach number at its exit is near sonic and attains the highest pressure/temperature with a minimum loss of stagnation pressure [1,2]. In high-speed flight, the propulsive power need varies greatly from take-off to cruise and finally landing; a fixed inlet configuration is unable to meet all these requirements. The desired performance is often obtained by a variable configuration inlet through a combination of compression ramps, unparallel sidewalls, and mass removing slots. In order to reduce the loss of stagnation pressure through shockwaves, the flow path also involves a multiple shock wave system to minimize the undesirable entropy jump through a single shock. The ideal isentropic compression is however unattainable. All these mechanical flow control devices lead to significant weight penalty and when operating beyond their design condition become parasitic [2]. Therefore an alternative to

these mechanical devices with a non-intrusive, rapid response flow control mechanism should be very appealing.

Resler and Sears [3] have advocated flow control using plasma as early as the late 1950's. The most attractive aspect of their ideas is introducing the electromagnetic forces as an expanding physical dimension for flow field manipulation. More recently Chernyi [4] has provided an interesting assessment on magnetohydrodynamic applications for high-speed flow control. Bityurin et al [5] also conducted extensive experimental studies on the flow field structure and the propagation of shock waves in inhomogeneous plasma. Most recently, Lennov et al [6] have investigated the basic mechanism of plasma and aerodynamic interaction near a solid surface. Innovative ideas have also been put forward for hypersonic flow control including thrust vectoring with and without an externally applied magnetic field [7-9].

A unique approach for integrating electromagnetic perturbations and viscous-inviscid interactions for hypersonic flow control has proven to be effective by a series of numerical simulations and experimental measurements [10-13]. The basic premise is built on the pressure interaction theory of Hayes and Probstein [14] that describes the viscous-inviscid interaction near the sharp leading edge of a solid surface. In supersonic flows, the slope of the displacement thickness of a shear layer, $\partial\delta^*/\partial x$, deflects the oncoming stream away from the solid surface, induces a series of compression waves and coalesces into an oblique shock. The induced surface pressure beneath the oblique shock can be calculated easily by the tangent-wedge approximation, the key parameter of the pressure interaction is defined as $\chi=(C/Re)^{1/2}M_\infty^3$. Depending on the combination of the free stream Mach number and Reynolds number based on the running distance from the leading edge, the pressure interaction is further classified as a strong or weak pressure interaction according to whether the value of χ is either greater or less than 3. The major difference is that for the strong pressure interaction the growth rate of the shear layer is altered by a strong favorable pressure gradient, $\nabla p \leq 0$, to grow proportional to $x^{3/4}$, instead of $x^{1/2}$ for laminar flows. The basic idea of the present approach is that an aerodynamic force of flow control can be derived from an electromagnetic surface perturbation that increases the slope of the shear-layer displacement for the viscous-inviscid interaction. This chain of events in turn produces a higher surface pressure for flow control. [10-11].

This concept has fully demonstrated its viability as a magneto-fluid-dynamic (MFD) flow control mechanism in the side-by-side experimental and computational investigations [10-13]. Following this idea; the present effort applies the amplified viscous-inviscid interaction near the leading edge of a rectangular inlet to act as a MFD compressor. For the present experimental investigation, a direct current discharge (DCD) is adopted as the plasma actuator. The electrodes of the DCD are embedded in the sidewalls of a constant cross-section area inlet; this arrangement is non-intrusive when deactivated. Once the discharge is actuated the combined volumetric Joule and conductive surface heating thickens the local displacement thickness. The increased slope of the displacement thickness through a viscous-inviscid interaction generates a series of compression waves and coalesces into an oblique shock. The compression is directly controlled by the power input to plasma generation of the electromagnetic perturbation. A high compression is automatically generated by the pressure interaction near the leading edge and is a strong function of the free stream Mach number.

For present purpose the electromagnetic perturbation via a DCD is imposed on the shear layer, and the combined volumetric Joule and convective electrode heating is the principal mechanism of disturbance. However, the plasma actuator can be replaced by a dielectric barrier discharge (BDB) or microwave radiation [15-17]. Using these electromagnetic perturbations, and in the presence of an externally applied magnetic field, additional electromagnetic forces such as the electrostatic and Lorentz accelerations can play an enhancing role. The oscillatory perturbation is also not a critical concern as long as the time scales of perturbation are much shorter the characteristic time frame of the fluid motion [15,16].

To demonstrate the viable concept of the MFD compression, a side-by-side experimental and computational investigation becomes necessary. The experiments are conducted in a plasma channel with a nominal Mach number of 5.15, and the computational results are obtained by solving the three-dimensional, compressible Navier-Stokes and magneto-fluid-dynamic equations with a weakly ionized air

model. The major emphasis of the present effect is focused on experimental observation and which is the start of a validating database for future research and development.

II. Experimental Conditions

All experimental investigations are conducted in a nominal Mach five magneto-hydrodynamic channel of the Air Force Research Laboratory [12,13]. This hypersonic low-density tunnel is a blow-down, free-jet facility. The rectangular cross-section nozzle with a throat area of 7.34×5.08cm expands to the nozzle exit plane of 7.34×17.78 cm. The test section currently in use has the dimension of 17.78×22.86×7.34 cm (L×H×W) [18]. Therefore the rectangular inlet model is limited to a dimension of 10.16×3.81×3.11 cm. The four sidewalls of the model have sharp leading edges with an outside bevel angle of 20 degrees. The electrodes embedded in the Phenolic vertical sidewalls are made of copper and the horizontal sidewalls are constructed of Plexiglas. The sketch of the tested model and the installation of the model in the hypersonic MHD channel are presented in Figures 1 and 2.

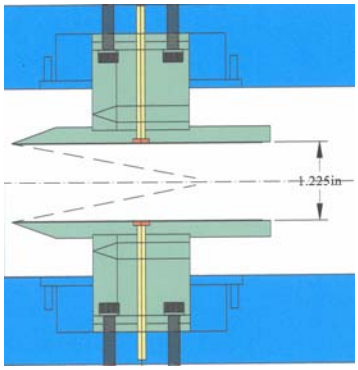

Figure 2. Model installation

In the preliminary study, the copper cathode and anode are embedded in opposite sidewalls parallel to the z coordinate. Therefore the gap distance between the electrodes is 3.11 cm. direct current discharge is sustained by the electric field strength up to 800 V for electrical currents of 40 and 80 mA. The electrodes are placed at a short distance of 0.64 cm downstream of the leading edge of the inlet to enhance the pressure interaction. The anode has half the width of the cathode in the streamwise direction (1.74 cm). In addition to this electrode arrangement, the second electrode configuration had an anode and a cathode on each side of the sidewalls. The discharges are now parallel to the surfaces. Most of the experimental data are collected for this configuration, where all electrodes have the identical dimensions of 3.175×0.64×0.16 cm, (length×width×depth). The cathodes are placed at short distance of 0.79 cm downstream from the leading edge of the inlet, and the distance between the centerline of the cathode and anode is 2.22 cm. In order to make comparison between the diffusive discharges, the electric field strength and current in the circuit remain nearly identical for the two different electrode arrangements [12,13]. The electrical current density on the anode of the cross channel discharge is 25.16 mA/cm^2 and the value is 21.27 mA/cm^2 for the discharge along the sidewalls.

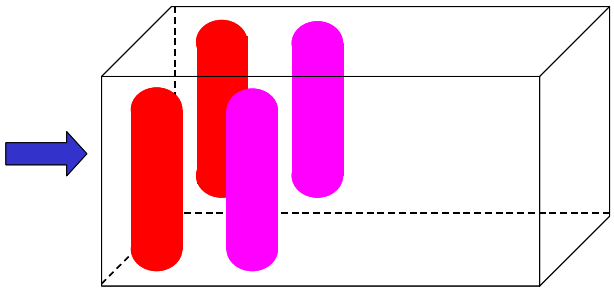
Figure 1. Sketch of inlet model, cathodes and anodes (3.175×0.64 cm)

The simulated altitude based on the static density range is from 30,000 to 50,000 meters. At a fixed stagnation temperature of 270 K and an unperturbed free stream Mach number of 5.15, the static temperature of the free jet is 43 K and a free stream velocity is 675.5 m/s. To ensure a stable inflow environment, tests are conducted at two stagnation pressures of 370 and 580 Torr. The incoming air stream has a static pressure of 0.59 or 0.92 Torr, and density of 6.4×10^{-3} or 10.03×10^{-3} kg/m^3 according to the different stagnation pressures. These conditions produce two Reynolds number based on the model length of 1.64×10^5 and 2.57×10^5 respectively. At this hypersonic Mach number and relatively low Reynolds number, the flow field is considered to be laminar.

The direct current discharge (DCD) is powered by a Universal Voltronics BRC-10-1000R-STD-3PH-208V reversible polarity switching power supplies. The maximum output is rated at 8 kW with a 10 kV output voltage at a signal impedance of 10 k Ohm. At the breakdown voltage of 800 V, a diffusive discharge is

achievable for plasma currents as high as 120 mA. For the two-pair electrode placement on parallel sidewalls, the total discharging area is 7.72 cm^2 representing only 5.48% of the total sidewall surface area.

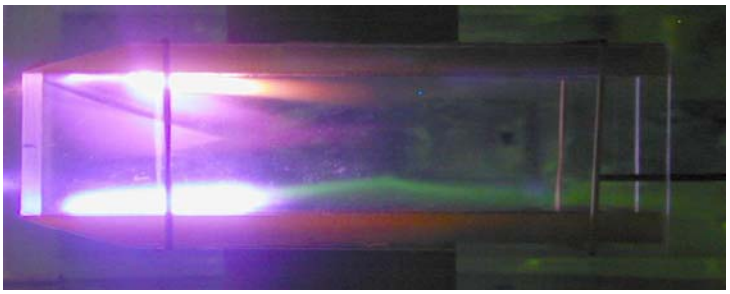

Figure 3. Discharge across inlet sidewalls, E=650V, I=40 mA

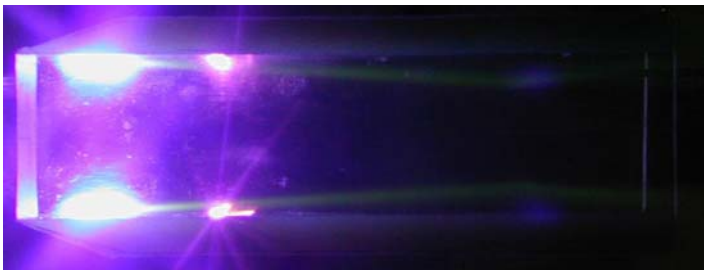

Figure 4. Discharge along inlet sidewalls,E=650V, I=40 mA

The discharging patterns of both electrode arrangements are given in Figure 3 and 4. Figure 3 presents the photographic top view of the flow field within the inlet with the actuating DCD across the sidewalls. Similarly, Figure 4 depicts the DCD along the sidewalls. Both discharges are generated by electrical field intensity from 600 to 800 V and an electric current from 40 to 80 mA by the same power supply unit. Since the electro-magnetic field is introduced into the flow field as a small perturbation, the basic flow structure is unaltered. The only changes are reflected by the stronger oblique shock waves. This modification is detectable by the steeper shock angle originating from the leading edges of the inlet. As a consequence, the shock intersection points move upstream, and most importantly the static pressure at the exit plane of the inlet is higher than when the DCD is deactivated.

Menart et al [19] and Kimmel et al [20] have thoroughly surveyed the weakly ionized air in the plasma channel using emission spectroscopy, microwave absorption, as well as a double Langmuir probe. For a normal glowing DCD and over a wide range of electrode arrangements with discharge currents up to 400 mA, the rotational and vibrational temperatures of the air plasma are scattering around 150 K and 5000 K. The maximum ion number density is also determined to be 8×10^{11}/cc, and the electrical conductivity is less than 1 mho/m near the electrode. At the lower stagnation pressure condition, the air number density is 1.33×10^{17}/cc, thus the mass fraction of the charged particles is less than 10^{-5}. At the higher stagnation pressure condition, the mass fraction is even lower. It is therefore justifiable that the nonequilibrium thermodynamics and chemical kinetics have not been taken into consideration in the present study.

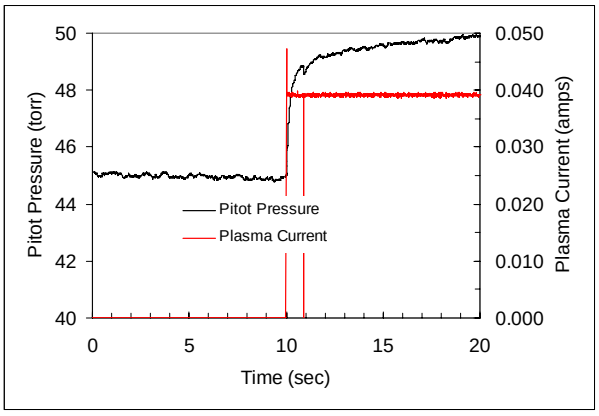

Figure 5. Typical data collecting process

A three-dimensional traverse mechanism has been developed for the facility for flow field survey [18]. This device has a freedom of movement to cover the entire domain of the test section. The placement of the traverse is controllable within a distance of 0.25mm. In the present effort, the collected data include only the Pitot pressure measurements and optical observations. A stainless steel Pitot probe has outer and inner diameters of 1.59 and 1.27 mm respectively. All pressure measurements were collected by a HP 385A data acquisition and control system. A single pressure transducer was used to collect all data. The Baratron MKS model 722A-23320 absolute pressure gauge has a calibrated accuracy of 0.1% of the 100 Torr full range.

The typical data collection is shown in Figure 5. The MHD channel is operated in a continuous and steady flow condition at a preset stagnation condition. The DCD is then ignited and the discharge is maintained at a constant current. The initial phase of the pressure response is on a fraction of a second time scale, then the conductive electrode heating effect appears [12,13,19,20]. The surface discharge electric current exhibits a random, low-amplitude (±0.2%), and continuous fluctuation (for the present tests, the measured spectrum is limited to 1.5 kHz). Therefore, the collected data are the time-averaged value over the sampling period. The Pitot pressure data is monitored for the entire data collection period of twenty seconds and continuously recorded. This data collecting procedure is standardized for the entire experimental effort.

III. Numerical Procedure

The magnetic Reynolds number, R_m, based on the experimental conditions is 8.48×10^{-6}. Under this circumstance, the low magnetic Reynolds approximation prevails, and the governing equations are [21]:

$$\partial\rho/\partial t+\nabla\cdot(\rho\mathbf{u}) = 0 \qquad (1)$$

$$\partial\rho\mathbf{u}/\partial t + \nabla\cdot(\rho\mathbf{uu} - \boldsymbol{\tau}) = \mathbf{J}\times\mathbf{B} \qquad (2)$$

$$\partial\rho e/\partial t + \nabla\cdot(\rho e\mathbf{u} - \mathbf{q} - \mathbf{u}\cdot\boldsymbol{\tau}) = \mathbf{E}\cdot\mathbf{J} \qquad (3)$$

Since the resultant governing partial differential equation system is identical to the Navier-Stokes equations except the non-zero source terms. The initial values and boundary conditions, as well as, the numerical procedure are directly usable from the cumulative knowledge of the CFD discipline [22,23].

The added electromagnetic effect of the flow is primarily derived from the electrically conducting medium. For most plasma actuators used for flow control, the weakly ionized gas is generated by electron collisions [24,25]. For the present purpose, the only required information for numerical simulation are the transport properties of the weakly ionized gas to describe the applied electrical field intensity, **E**, and electrical current density, **J**, in the basic formulation, equations (2) and (3).

A model of a three-component plasma (neutral, electron, and ion) and two-temperature plasma of the present formulation based the drift-diffusion theory are adopted to evaluate the total energy release into the air stream [23]. A compatible electrical field intensity, **E**, in the discharge domain is obtained by satisfied the well-known Poisson equation of plasmadynamics involving the space charge. For computation using a simple phenomenological weakly ionized air model, only the Joule heating rate is needed [9-11].

The basic solving scheme of the governing equations in conservative variables (ρ, ρu, ρv, ρw, ρe) is a semi-discrete, finite-volume algorithm [26,27]. The upwind-biasing approximation is applied to the convective and pressure terms and central differencing is used for the shear stress and heat transfer terms. In other words, a flux splitting formulation is used; the flux vectors at the control surface are written as an exact solution to the approximate Riemann problem. In order to control the discontinuous pressure jumps at the shock front, the min-mod limiter is adopted for the present computations.

All numerical simulations are generated on two mesh systems: (85×81×45) and (105×101×57). The minimum grid spacing immediately adjacent to the sidewall is one hundredth of the laminar boundary thickness at the inlet exit. The grid spacing is stretched from the inlet sidewalls toward the centerline by a geometric constant of 1.05. Clustered mesh spacing is also implemented at the leading edge of the inlet; four streamwise cross-section planes are set upstream of the leading edge to describe the unperturbed free stream. The streamwise grid spacing is then stretched from the leading edge toward downstream. For the present analysis, the iterative convergence is accelerated through a multi-grid technique using a three-level mesh sequencing [27]. The data processing rate on a 400 Mhz SGI Octane2 workstation is 61.6×10^{-6} seconds per number of cells per number of iteration. The convergence criterion of the present analysis is preset at a value of 3.0×10^{-7} of the normalized global residue. A coarse grid solution attains its steady state asymptote after 300 iterations requiring 5400 seconds.

IV. Flow Field Structure

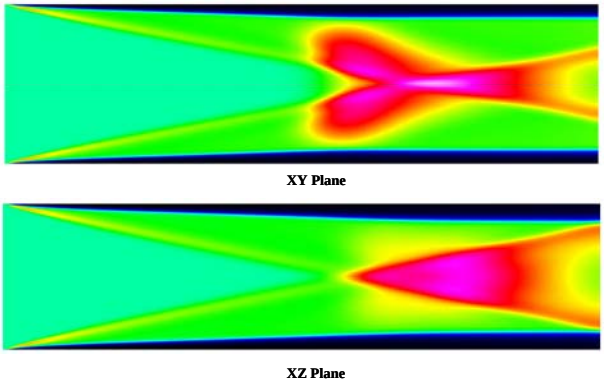

Figure 6. Density contours in xz and xy central planes

The flow field structure of the simple rectangular inlet is surprisingly complex. Four equal strength oblique shocks emanate from the mutually perpendicular sharp leading edges. These shocks are the result of the weak pressure interaction near the hypersonic leading edges, and the peak pressure at the leading edge is as high as 4.2 times the free-stream value, and expands downstream. The coalesced shocks from the entrance of the inlet have a deflection angle of 11.7 degrees. The four shocks do not intercept each other at the same streamwise location, because the width of the inlet is shorter than the height, so the oblique shocks over the vertical sidewalls intercept each other at x/L=0.50. The intersection of the oblique shocks over the horizontal sidewalls is located at x/L=0.54. At these locations, shock-on-shock interaction also takes place. The shock wave structure is clearly discernable from the computed density contours shown in Figure 6 which duplicates the experimental conditions. Downstream of the intersections, all shocks continuously propagate, reflect from the sidewalls, and eventually exit the inlet.

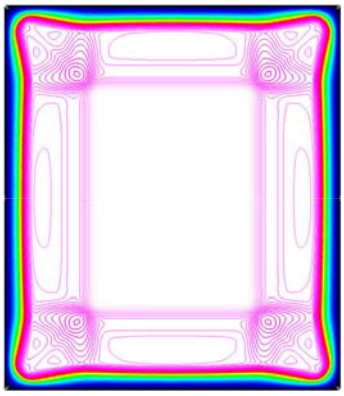

Figure 7. Triple-points shock formation in cross-flow plane at x/L=0.25

Upstream of the shock intersections, connecting shock waves must exist between the two perpendicular families of shocks parallel to the y and z coordinates in order that the continuity condition is satisfied [28]. Therefore, there are a total of eight triplet points in the shock wave formation in each cross-sectional plane. In Figure 7, the Mach number contours at the streamwise location of x/L=0.25 from the inlet leading edge are depicted. Although all oblique shocks are relatively weak, the numerical solution captures this peculiar shock structure. The multiple shock compression in the corner region is clearly reflected through the thinning of the viscous layer as it enters these domains.

V. Discharge across Sidewalls

In the early phase of the experimental effort, the DCD is applied across the vertical walls of the inlet. The discharging column has a height identical to the width of the inlet, 3.11 cm. After the initial breakdown, the DCD is maintained at the electrical field intensity no more than 820 V for an external circuit current up to 80 mA. Both of the electrodes are placed a short distance of 0.64 cm downstream of the leading edge to enhance the pressure interaction. The copper cathode has a dimension of 2.54×2.54×0.16 cm (length×width ×depth), thus a discharging surface area of 6.45 cm^2. The anode has the half width of the cathode in the streamwise direction (1.74 cm). Although the discharging pattern is fully understood [23], the difference in electrode surface areas and electrical field intensity due to the cathode fall may lead to an asymmetrical electromagnetic perturbation. For this reason, a limited

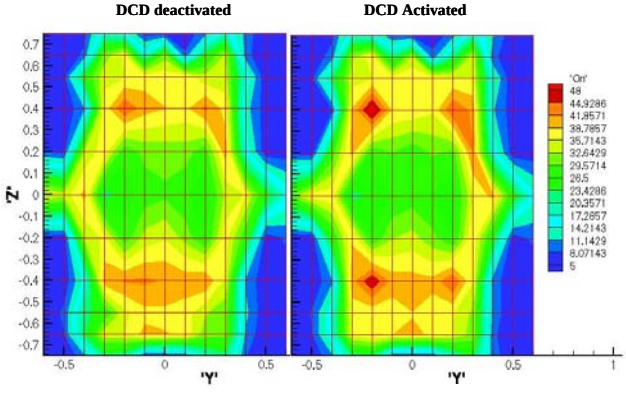

Figure 8. Comparison of Pitot pressure contours with/without DCD (E=800V & I=40 mA)

numbers of tests were conducted for this particular electrode arrangement.

Figure 8 presents the measured Pitot pressure contours at a stagnation pressure of 370 Torr. At the streamwise location of x/L=0.75, the shocks originating from the sidewalls have already intercepted each other upstream and are propagating on a divergent path. Thus the shocks over the horizontal sidewalls are moving away from each other. The surface discharge is sustained at 650 V and 40 mA; the total power input for plasma generation is 26 watts. Since the DCD is introduced as a small perturbation to alter the flow field structure, the basic shock formation in Pitot pressure contours with and without the discharge is similar as anticipated. The most significant difference between the two tested conditions is that when the DCD is activated the vertical shocks are closer to each other because the steeper oblique shock angle. Meanwhile the value of the Pitot pressure at the shock front is elevated when DCD is actuated. The Pitot pressure data are collected by a probe with a finite external diameter and therefore have a limited traverse range near the sidewalls.

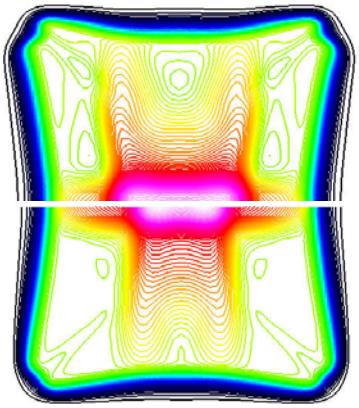

Figure 9. Computed Pitot pressure contours with/without DCD

The effect of an electromagnetic perturbation on the Pitot pressure distribution is better described by the numerical simulation than the experimental results under the identical condition, because of the much higher data point density (11514 versus 143). A composite drawing of the computed Pitot pressure contours in Figure 9 clearly highlights the interaction and agrees with the experimental observation. At the lower stagnation pressure tested, 370 Torr, the Pitot pressure of the unperturbed stream registers a value of 20.42 Torr and this is confirmed by measurements and computations. Based on this reference value the inviscid core still exists in the middle section of the inlet. From the experimental data and computational results this complex flow field structure within the inlet becomes traceable.

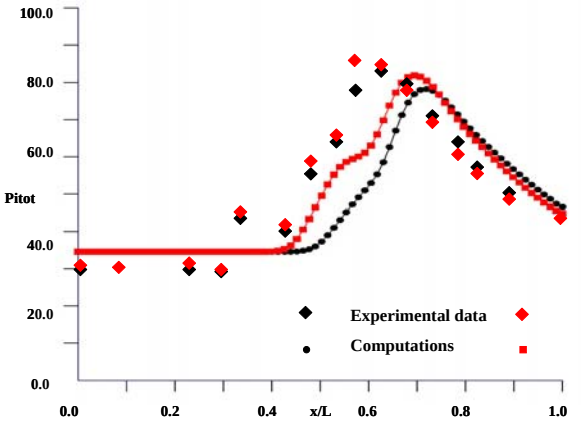

Figure 10. Comparison of Pitot data and computation at inlet centerline

Figure 10 depicts the experimental and computed results of Pitot pressures along the centerline of the rectangular inlet when the DCD is either actuated or deactivated. At the higher tested stagnation pressure of 580 Torr, the experimental and computational results reveal the consequence of interacting oblique shocks within the inlet. The DCD is maintained in the hypersonic inlet by an applied electric field intensity of 820 V between electrodes. When the DCD is actuated, the induced oblique shock becomes steeper, and advances the shock intersection upstream. The reduced Mach number behind the strengthened shock, and a higher local static pressure, produce a higher Pitot pressure value. The actuated DCD produces a higher static pressure than the deactivated counterpart. The computed results indicate an interacting pressure rise further downstream than the experimental observations. The probable causes of this discrepancy are tentatively identified to be the slightly blunt leading edge of the inlet model and a higher inlet Mach number due to the model blockage. The computations underpredict the peak Pitot pressure by 4% and overpredict the uniform entrance condition by 4.2%. This discrepancy in magnitude is directly attributable to the uncertain Mach number at the entrance of the inlet. Nevertheless, the agreement between the experimental data and computations is reasonable.

Since all experimental data are limited to the Pitot pressure measurements, the compression produced by the combined effect of electromagnetic perturbation and viscous-inviscid interaction can only be evaluated by computational simulation. The static and stagnation pressure distributions are deduced from the numerical results. It is found that the static pressure at the exit plane of the inlet is greater when the DCD is deactivated and the loss in stagnation pressure due to the stronger oblique shock is negligible. This result is the first demonstration that magneto-fluid-dynamic compression can be achieved in a rectangular constant cross-section inlet.

VI. Discharge along Sidewalls

A major portion of the experimental data is collected for the DCD along the parallel vertical sidewalls. A part of the reasons is that this electrode arrangement alleviates the possibility of an unsymmetrical electromagnetic perturbation and allows more power input to the plasma for a diffusive discharge. This electrode arrangement was successfully used for hypersonic flow control over a wedge model [11-13]. In those series of investigations, the plasma-induced surface pressure is equal to the compression of an oblique shock generated by a deflection angle of five degrees or more in a free-stream Mach number of 5.15. The compression beneath the oblique shock is 1.41 times the freestream value and the value increases to 2.23 at a Mach number of 10.

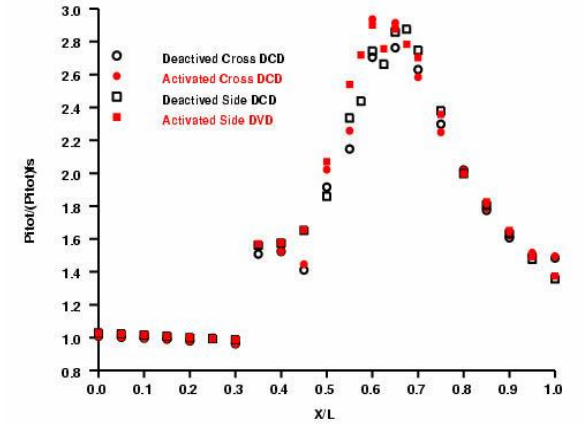

Figure 11. Comparison of DCDs cross and along sidewalls

A comparison of the streamwise Pitot pressure distributions under three different discharge conditions along the centerline of the rectangular inlet is given in Figure 11. When the DCD is deactivated, the measurements reveal a repeatability pattern upstream of the MFD interaction ($x/L < 0.3$). In this region, the Pitot pressure data essentially duplicated each other. The time-averaged data however exhibit a scattering band in the shock-shock and shock-shear-layer interacting zone to reveal an unsteady interaction behavior. At a data sampling rate of two hundred points per second, the maximum time-average data scatter of 6.3% occurs at the streamwise location $x/L=0.55$. In fact, the maximum difference in Pitot pressure measurements is of the same order of magnitude when DCD is actuated either across or along the sidewalls of the inlet. In any event, the Pitot pressure data is consistently higher when the DCD is actuated than deactivated. For the DCD across the inlet sidewall, the discharge is sustained by an averaged applied electric field of 820 V and at the electric current of 81 mA. The corresponding input to the side-by-side DCD is 745 V and 82.1 mA respectively. In this regards, the power input for plasma generation has a small difference from 61.16 to 66.42 W. The Pitot pressure distributions under the two difference electromagnetic perturbations are essentially identical within the data scattering band.

The pressure rise induced by the electromagnetic perturbation is a function of the power input for plasma generation. This control mechanism is demonstrated by reducing the power input from 61.16 W (745 V and 82.1 mA) to 24 W (600 V and 40 mA). In Figure 12, the effectiveness of this control mechanism is depicted in the streamwise Pitot pressure distributions. The flow conditions are identical except the difference in the DCD power input. The difference between the flows is the applied electric field intensity that leads to different electrical current densities; 21.6 mA/cm^2 versus 12.7 mA/cm^2.

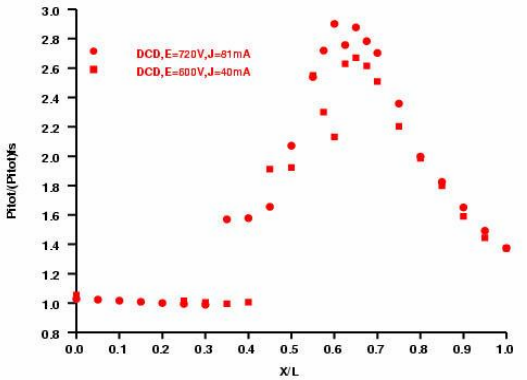

Figure 12. Effect of power input to MFD Interaction

For the Joule heating dominant MFD interaction, the term of **E·J** reduces by a factor of 2.11 resulting in a proportional but smaller 9.6% decrease in the maximum Pitot pressure rise. A higher power input for surface plasma generation of 120 mA at 940 V was also investigated. The experimental data exhibit a more drastic change, both in discharge characteristics and flow structure that requires repeatable measurements and further study.

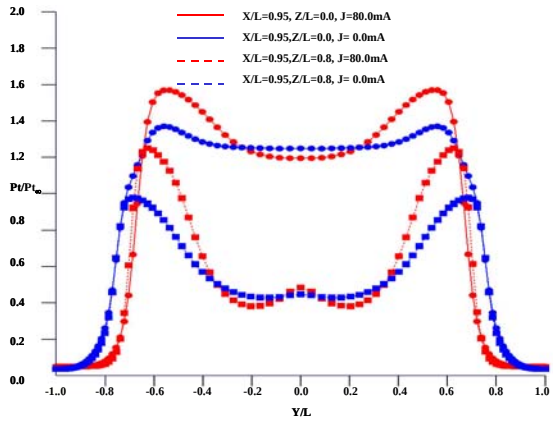

Figure 13. Computed Pitot pressure distributions with/without DCD, x/L=0.95

The magneto-fluid-dynamic interaction is best described by the cross flow formation that is induced by electromagnetic perturbation and subsequently amplified by viscous–inviscid interaction. A much clearer pictorial description can be provided by numerical simulations, which describe the changes with smaller data scatter. In Figure 13, the computed Pitot pressure distributions across the y coordinate near the inlet exit plane (x/L=0.95) are presented. The pressure distributions along the centerline (z/L=0.0) and close to the upper discharging surface (z/L=0.8) with and without an actuated DCD are depicted in this figure. The computed results indeed show that the electromagnetic perturbation produces a small perturbation to the shock wave structure at a relatively low hypersonic Mach number. The change of the flow field structure is most accentuated at the shock front and is fully substantiated by the experimental observation shown in Figure 8.

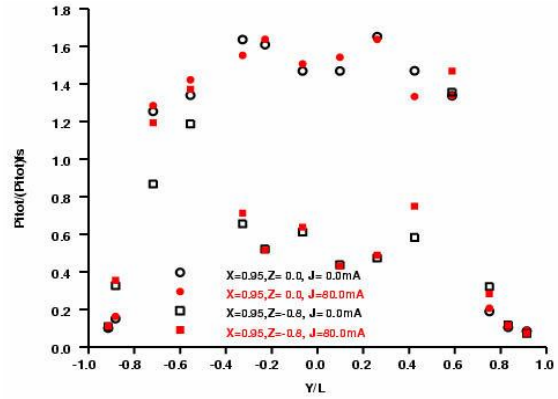

Figure 14. Pitot pressure profiles in cross-flow plane, x/L=0.95

The measured Pitot pressure data at the identical streamwise location is presented in Figure 14. The surface discharge when actuated is sustained with an applied electric field of 745±10 V and the electrical current at the electrode is 80±2 mA. The data are collected at the stremwise location of x/L=0.95. A total of four sets of data are shown across the width between the electrodes embedded sidewalls. Two sets of data are recorded at the same location on the y coordinate but with actuated and deactivated DCD. The data recording position does not always coincide with the location where the maximum difference occurs. The Pitot pressure data cross each other at different spanwise locations (see numerical results in Fig.13). Even with the measurement scatter, the data show a consistently higher value when the DCD is actuated.

This similar behavior is also noted in the upstream Pitot pressure survey at x/L=0.5, shown in Figure 15. At the central plane of the inlet, the oblique shocks originating from the horizontal sidewalls begin to intersect each other, and the shock-shock interaction produces a high Pitot pressure plateau near the centerline. The Pitot pressure profile off

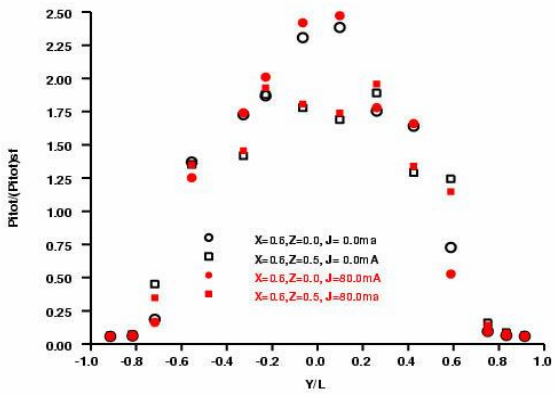

Figure 15. Pitot pressure profiles of cross-flow plane, x/L=0.5

the the centerline, z/L=0.5, captures the pressure plateau of intersected compression waves originating from the electrodes embedded sidewalls. The pressure with the actuated surface discharge is persistently higher than its deactivated conterpart. This pattern of Pitot pressure measurements is consistent over all experimental observations. The appearance of a random data scattering is in part reflected by the complex and weak shock-shock and shock-boundary-layer interactions. A better definition of the profile may be acquired by data collection at different locations for actuated and deactivated surface discharge or simply with a greater data density.

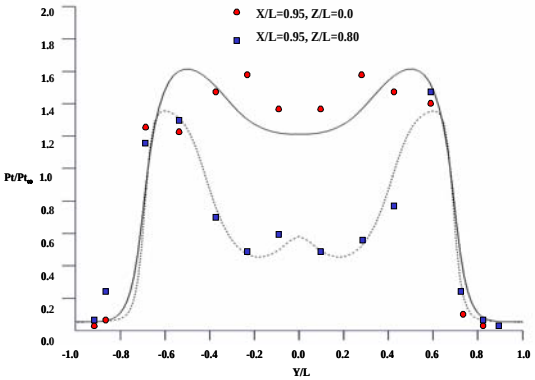

Figure 16. Calibrated computed Pitot pressure against experimental data

A quantitative assessment of the static pressure recovery from the magneto-compression within the inlet must rely on the numerical simulation. The computed result employed a plasma model which must first be calibrated against the experimental data. The comparison of the computed Pitot profiles near the inlet exit plane at x/L=0.95 is depicted in Figure 16. The numerical results not only duplicate the flow condition of the MHD channel, but also the placement of cathode and annode of the inlet model. Only an additional input of the electrode temperature for the numercial simulation is required. This temperature is assigned a value of 460 K in an attempt to mimic the experimental conditon [12,13]. The computed Pitot pressure distributions underpredict the peak values near the centerline but are in excellent agreement with data in the middle span.

The computed static pressure distributions with and without a DCD across the half z-span of the inlet central plane is presented in Figure 17. The basic static pressure distribution is similar to the Pitot pressure but without the accentuation of the Mach number variations. The characteristic of a strengthened shock-on-shock and shock-boundary interaction is clear revealed. The static pressure in the shear layer is uniformily higher and with a greater weak shock compression away from the center of the inlet than the flow without DCD. Integrating the computed static pressure distributions over the entire exit plane of the inlet with and without an activated surface discharge shows a net gain in magneto compression of 11.6 %. This additonal compression within a rectangular and constant cross-section area inlet is genertaed by a small power input for the surface plasma generation of 61.16 W, and at an entrance Mach number of 5.15. At an electrode length of 3.175 cm, the scaled power input is 19.21 W/cm based on the electrode length. These values of the required power for plasma generation and the gained compression are also nearly identical to earlier hypersonic flow control simulations [10-13].

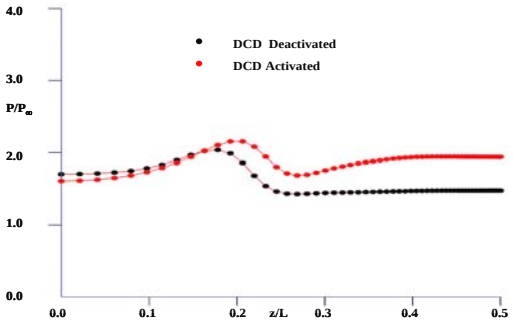

Figure 17. Static pressure distributions with/without DCD, x/L=0.95

VII. Conclusions

The magneto-fluid-dynamics interaction within a rectangular, constant cross-section area inlet achieves 11.6% greater pressure compression for the inlet with an entrance Mach number of 5.15 when the surface discharge is actuated. According to classic hypersonic pressure interaction theory, the compression will increase proportional to the cubic power of the entrance Mach number. Therefore, it has a viable application in hypersonic flows.

The electromagnetic force is introduced into the magneto-fluid-dynamics interaction as a small perturbation and amplified by the viscous-inviscid interaction. This chain-of-events is further substantiated by the two entirely different electrode arrangements. The net compressions are nearly identical; independent of whether the discharge is across or along the two inlet sidewalls

The reported magneto-fluid-dynamic interaction is characterized by low-amplitude and high frequency fluctuations. The source of the unsteady motion is linked to the oscillatory surface discharge behavior. The fluctuating electromagnetic perturbation generates a maximum time-averaged data scatter of 6.3%. It will be an interesting objective of future research to understand and suppress this measurement uncertainty.

VIII Acknowledgement

The sponsorship by Dr. John Schmisseur and Dr. Fariba Fahroo of the Air Force Office of Scientific Research is sincerely acknowledged.

IX References

1. Oates, G.C., Aerothermodynamics of Gas Turbine and Rocket Propulsion, 3rd edition, AIAA. 1997.
2. Kurth, G., Critical Physical Phenomena in Scramjet Propulsion, AGARD-CP-600, 2002, pp. C5.1-C5.11.
3. Resler, E.L., Sears, W.R., The Prospect for Magneto-aerodynamics, J. Aero. Science 1958, Vol. 25, 1958, pp. 235-245 and 258.
4. Chernyi, G.G., Some Recent Results in Aerodynamic Applications of Flow with Localized Energy Addition, AIAA 99-4819, Norfolk VA, Nov. 1999.
5. Bityurin, V., Kilmov, A., Leonov, S., Lutsky, A, Van Wie D., Brovkin, V., and Kolesnichenko, Yu., Effect of Heterogonous Discharge Plasma on Shock Wave Structure and Propagation, AIAA 99-4940, Norfolk VA, Nov. 1999.
6. Leonov, S.B., Yarantsev, D.A., Gromov, V.G., and Kuriachy, A.P., Mechanisms of Flow control by near-surface Electrical Discharge Generation, AIAA 2005-0780, Reno NV, January 2005.
7. Shneider, M.N., Hypersonic Aerodynamic Control and Thrust Vectoring by Nonequilibrium Cold-Air MHD Devices, AIAA 2005-0979, Reno NV, January 2005.
8. Borghi, C.A., Carraro, M., and Cristofolini, A. An Axi-symmetric Hall Configuration for the MHD Interaction in Hypersonic Flows, 2005-4785, Toronto Canada, June 2005.
9. Gaitonde, D.V., Simulation of local and Global High-Speed Flow Control with Magnetic Field, AIAA 2005-0560, Reno NV, January 2005.
10. Shang, J.S. and Surzhikov, S.T., Magnetoaerodynamic Actuator for Hypersonic Flow Control, AIAA Journal Vol. 43, No. 8, August 2005, pp. 1633-1643.
11. Shang, J.S. Surzhikov, S.T., Kimmel, R. Gaitonde, D.V., Hayes, J.R., and Menart, J., Plasma Actuator for Hypersonic for Flow Control, AIAA 2005-0652, Reno NV. January 2005.
12. Menart, J. Shang, J.S., Kimmel, R., and Hayes, J. Effects of Magnetic Fields on Plasma Generated in Mach 5 Wind Tunnel, AIAA 2003-4165, Reno NV, Jan. 2004.
13. Kimmel, R, Hayes, J., Menart, J., and Shang, J.S., Effect of Surface Plasma Discharges on Boundary Layer at Mach 5, AIAA 2004-0509, Reno NV, Jan. 2004.
14. Hayes, W.D., and Probstein, R.F., Hypersonic Flow theory, Academy Press, 1959.
15. Shang, J.S. Electromagnetic Field of Dielectric Barrier Discharge, AIAA 2005-5182, Toronto Canada, June 2005.
16. Boeuf, J.P., and Pitchford, L.C., Electrohydrodynamic Force and Aerodynamic Flow Acceleration in a Surface Dielectric Barrier Discharge, J. Applied Physics Vol. 97 May 2005, pp.103307-1-10.
17. Kolesnichenko, Y., Selected Topics of Physics and Diagnostics of MV Discharge, AIAA 2005-0405, Reno NV, January 2005.
18. Shang, J.S., Kimmel, R. Hayes, J., Tyler, C., and Menart, J., Hypersonic Experimental Facility for Magneto-Aerodynamic Interactions, J. Spacecraft and Rocket, Vol. 24, No. 5, 2005, pp.
19. Menart, J.A., Shang, J.S., Henderson, S., Kurpik, A., Kimmel, R., and Hayes, J. Survey of Plasma Generated in a Mach 5 Wind tunnel, AIAA 2003-1194, Reno NV, January 2003.

20. Kimmel, R.L., Hayes, J.R., Menart, J.A., Shang, J., and Henderson, S., Measurements of a Transverse DC Discharge in a Mach 5 Flow, AIAA 2003-3855, Orlando FL. June 2003.
21. Mitchner, M. and Kruger, C.H. Jr. Partially Ionized Gases, John Wiley & Sons, 1973, pp.188-198.
22. Shang, J.S. and Surzhikov, S.T., Magnetoaerodynamic Actuator for Hypersonic Flow Control, AIAA Journal Vol. 43, No. 8, August 2005, pp. 1633-1643.
23. Surzhikov, S.T. and Shang, J.S. Two-Component Plasma Model for Two-Dimensional Glow Discharge in Magnetic Field, J. Computational Physics, Vol. 199, 2, Sept. 2004, pp. 437-464.
24. Howatson, A.M., An Introduction to Gas Discharges, Pregamon Press, Oxford, 1975, pp. 51-83.
25. Raizer, Yu. P., Gas Discharge Physics, Springer-Verlag, New York, 1977.
26. Rumsey, C., Biedron, R., and Thomas, J., CFL3D: Its History and Some Recent Applications, NASA TM-112861, May 1007.
27. Thomas, J.L., Diskin, B., Brandt, A., Textbook Multigrid Efficiency for Fluid Simulation, Annual Review of Fluid Mechanics, Vol. 35, January 2003, pp.317-340.
28. Shang, J.S. and Hankey, W.L., Numerical Solution of the Navier-Stokes Equations for a Three-Dimensional Corner, AIAA J., Vol. 15, No. 11, 1977, pp. 1675-1582.